ACS Energy LETTERS

http://pubs.acs.org/journal/aelccp

LETTER

Stable Hexylphosphonate-Capped Blue-Emitting Quantum-Confined $CsPbBr_3$ Nanoplatelets

Javad Shamsi, Dominik Kubicki, Miguel Anaya, Yun Liu, Kangyu Ji, Kyle Frohna, Clare P. Grey, Richard H. Friend, and Samuel D. Stranks*

Cite This: *ACS Energy Lett.* 2020, 5, 1900−1907

Read Online

ACCESS | Metrics & More | Article Recommendations | Supporting Information

ABSTRACT: Quantum-confined $CsPbBr_3$ nanoplatelets (NPLs) are extremely promising for use in low-cost blue light-emitting diodes, but their tendency to coalesce in both solution and film form, particularly under operating device conditions with injected charge-carriers, is hindering their adoption. We show that employing a short hexylphosphonate ligand ($C_6H_{15}O_3P$) in a heat-up colloidal approach for pure, blue-emitting quantum-confined $CsPbBr_3$ NPLs significantly suppresses these coalescence phenomena compared to particles capped with the typical oleyammonium ligands. The phosphonate-passivated NPL thin films exhibit photoluminescence quantum yields of ∼40% at 450 nm with exceptional ambient and thermal stability. The color purity is preserved even under continuous photoexcitation of carriers equivalent to LED current densities of ∼3.5 A/cm^2. ^{13}C, ^{133}Cs, and ^{31}P solid-state MAS NMR reveal the presence of phosphonate on the surface. Density functional theory calculations suggest that the enhanced stability is due to the stronger binding affinity of the phosphonate ligand compared to the ammonium ligand.

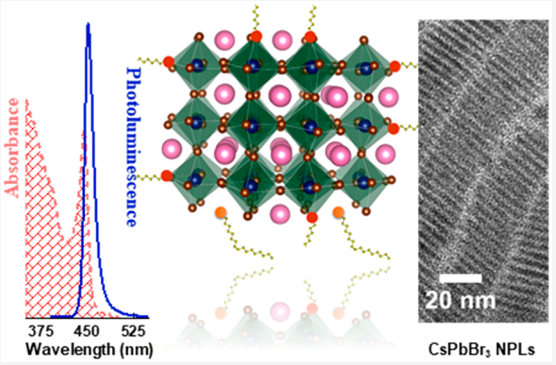

The search for a low-cost alternative to the current state-of-the-art gallium-nitride-based emitters for blue light-emitting diodes (LEDs)3 is key to revolutionizing the lighting and display sectors.[1,2] For this goal, achieving high-quality optical properties in strongly quantum-confined luminescent nanocrystals (NCs) is an enduring challenge for their commercialization. Lead halide perovskite (LHP) NCs such as $CsPbX_3$ (X is a halide) have potential to be disruptive players in this space.[3,4] These materials possess superlative optoelectronic properties, such as narrow emission line widths (full width at half-maximum (fwhm) < 150 meV), tunable bandgaps (ranging from ultraviolet to near-infrared), high exciton binding energy, and defect tolerance.[5] The high color purity and wide color gamut make LHP NC-based LEDs particularly promising for next-generation display applications.[6−10]

In general, there are three synthesis routes to achieve colloidal suspensions of blue-emitting $CsPbX_3$ NCs:[5] (i) halide engineering, i.e., using mixtures of Cl and Br; (ii) downsizing the $CsPbX_3$ cuboids to 2−5 nm; and (iii) forming anisotropic quantum-confined nanoplatelets (NPLs). Among them, the last approach has so far delivered photoluminescence quantum yield (PLQY) of near unity for pure blue-emitting $CsPbBr_3$ NPLs ($\lambda_{emission}$ = 450−465 nm) in solution, though this value drops once the NPLs are deposited as thin films because passivation strategies such as maintaining excess bromide are not as effective in the solid state.[11−13] Furthermore, the photoluminescence (PL) of these $CsPbBr_3$ NPLs shift from the blue (450−465 nm) to the green (500−520 nm) over time because of the coalescing of NPLs and subsequent loss of quantum confinement.[14,15] This phenomenon is due to the labile interaction of the primary amine capping ligands (e.g., oleylamine, OLA) on the surface as an A-site cation with the perovskite lattice.[15−17] Such primary amines are crucial for the formation of anisotropic LHP NPLs:[5] varying the ratio of Cs to OLA^+ is a key experimental parameter for reducing the thickness of $CsPbBr_3$ NPLs down to the few monolayers that are sufficiently thin to achieve quantum confinement.[12,18,19]

Received: April 29, 2020
Accepted: May 15, 2020
Published: May 15, 2020

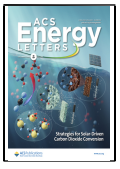

Hence, there is a critical need to explore new capping ligands to address optical stability while keeping their quasi-two-dimensional confined characteristics intact. Although several groups recently investigated the role of different capping ligands to address low PLQY values and/or poor optical stability (e.g., using phosphonic acid),[20−23] all works to date have focused on green-emitting $CsPbBr_3$ cuboids,[24−26] and there are to date no reports of successful approaches for truly confined NPLs.

Here, we exploit the beneficial properties of OLA in forming anisotropic NPLs but then use a short phosphonate ligand (hexylphosphonic acid, HPA) that successfully competes with the labile OLA ligand to form highly stable, quantum-confined $CsPbBr_3$ NPLs. We achieve both high PLQY in the solid state (~40%) at a true display blue emission energy (~450 nm) but also suppress the coalescence of NPLs in both solution and thin films even under high densities of photoinjected charge carriers (equivalent to an LED operating at ~3.5 A/cm^2).

Direct colloidal synthesis of $CsPbBr_3$ NCs using only a phosphonate ligand does not lead to the formation of anisotropic NPLs.[20] In our initial scheme, we employed HPA to modify the surface of $CsPbBr_3$ NPLs through a postsynthetic treatment. The pristine NPLs were synthesized based on a heat-up method previously reported by Shamsi et al. in which OLA and oleic acid (OA) were used to dissolve $PbBr_2$, and the resulting NPLs are OLA-passivated (OLA-NPLs; see Experimental Section in the Supporting Information for details).[27,28] We observed that the addition of a small amount of HPA (dissolved in toluene) to the OLA-NPL solution resulted in green-emitting impurities (see Figure S1). We resolved these issues by adopting an *in situ* surface passivation strategy by adding HPA/isopropanol to the precursor solutions (Experimental Section in the Supporting Information). The excitonic absorption band at 445 nm and PL peak at 450 nm with a fwhm of 15 nm validate the formation of $CsPbBr_3$ NPLs (Figure 1a).

A transmission electron microscopy (TEM) and high resolution TEM images of a typical sample of $CsPbBr_3$ NPLs synthesized with our approach are reported in Figures 1b and S2a, respectively. The NPLs were characterized by stacks of face-to-face aligned NPLs, with the particles typically oriented perpendicularly with respect to the carbon support film (see the scheme in Figure S2b), which enabled a precise estimation of the NPL thickness. The NPLs had a thickness of 2.4 ± 0.3 nm (corresponding to 4 unit cells)[19,29] and average lateral dimensions of 6 ± 2 nm × 26 ± 5 nm. We note that the dimensions of these HPA-NPLs, along with the PL and absorption peaks, are similar to those of the OLA-NPLs (Figure S3), suggesting that the addition of HPA does not significantly influence the nucleation and growth process of NPLs in the modified scheme used here. An X-ray diffraction (XRD) pattern from a $CsPbBr_3$ HPA-NPL thin film sample is reported in Figure 1c. The pattern agrees with the bulk orthorhombic $CsPbBr_3$ reference (black), with small shifts owing to surface ligands modulating the lattice. The peaks at 2θ = 15° and 29.7° are particularly intense owing to the anisotropic and defined orientations of the NPL facets.[30]

In our proposed passivation mechanism, the amount of HPA is critical for the resulting optical properties. We found that the PLQY shows an increase from 25% when HPA/Pb = 0 (OLA-NPLs) to ~40% when HPA/Pb = 1.5 for $CsPbBr_3$ NPL thin films, indicating that radiative recombination pathways are more effectively out-competing nonradiative pathways in the

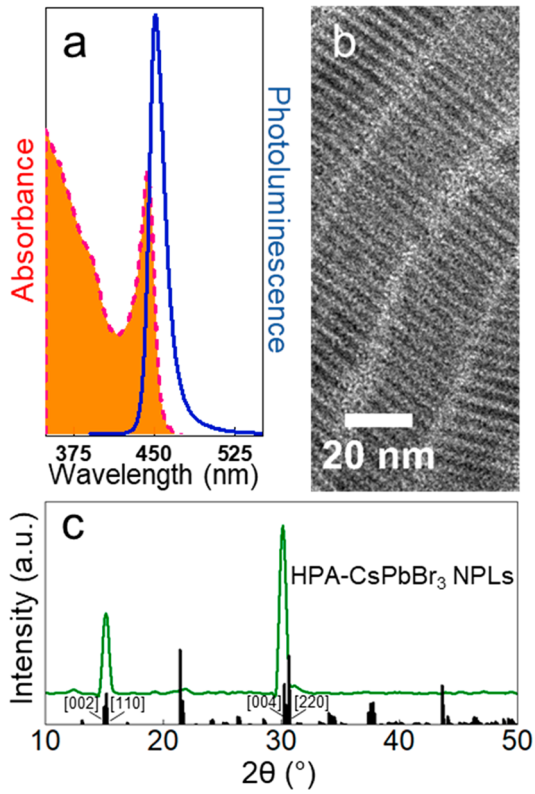

Figure 1. HPA-$CsPbBr_3$ NPL thin films: (a) optical absorbance and PL of a colloidal solution, (b) TEM image, and (c) XRD pattern. The black pattern in panel c is the ICSD reference 980097851, representing the bulk orthorhombic $CsPbBr_3$ phase, with key peaks assigned.

HPA-NPLs. Higher HPA/Pb ratios result in a broad PL peak in the green range (Figure S4). PL decay measurements on thin films of both compositions reveal excitonic-like recombination in both cases as the recombination does not change with fluence (Figure S5). Multiexponential fits[31] to the decays reveal the average lifetime decreases from 4.96 ns (OLA-NPL) to 3.68 ns (HPA-NPL) (see Figure S5 for fits and fitting parameters). Higher PLQY, together with faster PL decay, indicates an increase in the radiative rate of the material, which likely relates to the changed material capping properties (Figure S5 and subsequent results). The more symmetric PL and the ~25 meV narrower emission fwhm of the HPA-NPLs compared to the OLA-NPLs (Figure S6) further support the higher optoelectronic quality of the HPA-NPLs.

In order to assess the purity and atomic-level microstructure of the HPA-NPLs, we carried out liquid- and solid-state nuclear magnetic resonance (NMR) measurements, which have recently been effectively used in lead halide perovskite[32−35] and inorganic nanocrystals.[36−38] ^{1}H liquid-state NMR spectra show that the HPA-NPLs only contains trace residual 1-octadecene (ODE) (Figure S7). Figure 2a shows the ^{31}P liquid-state spectra of HPA and HPA-NPLs. HPA yields a singlet at 40.1 ppm (fwhm 5 Hz), consistent with rapid isotropic reorientation of HPA. On the other hand, the solution of HPA-NPLs yields a considerably broader signal at 34.7 ppm (fwhm 79 Hz), confirming that in this case the phosphonate species are different than those in the pure HPA sample. The broadening is consistent with faster T_2 relaxation because of slower molecular reorientation (i.e., longer correlation times) of the NPL-bonded ligand, as has been

https://dx.doi.org/10.1021/acsenergylett.0c00935
ACS Energy Lett. 2020, 5, 1900−1907

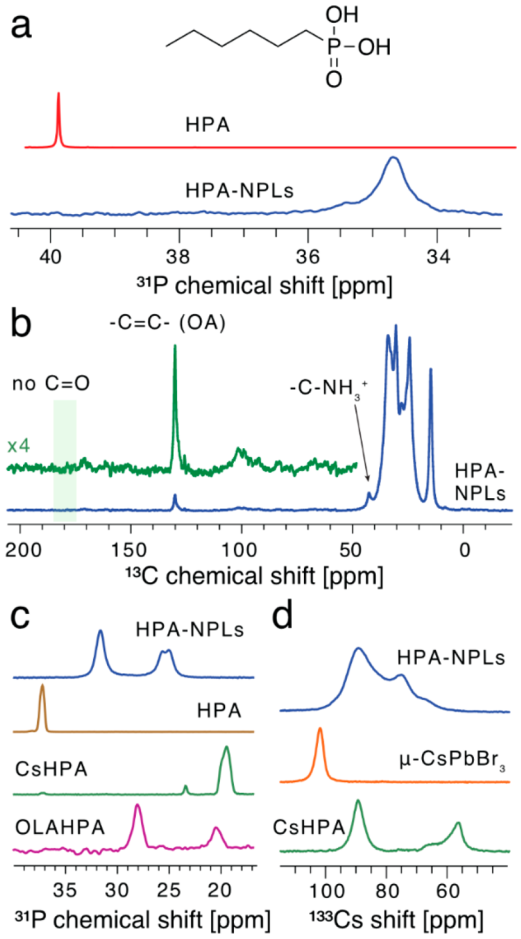

Figure 2. NMR characterization of the materials. The structure of *n*-hexylphosphonic acid (inset). Liquid-state (a) ^{31}P NMR spectra in toluene-d_8 at 11.7 T of *n*-hexylphosphonic acid (HPA) and HPA-capped $CsPbBr_3$ nanoplatelets (HPA-NPLs). Solid-state MAS NMR at 16.4 T and 12 kHz MAS (unless stated otherwise): (b) ^{1}H−^{13}C CP spectrum of HPA-capped $CsPbBr_3$ NPLs. (c) ^{1}H−^{31}P CP MAS NMR spectra of HPA-capped $CsPbBr_3$ NPLs, neat HPA (at 20 kHz MAS), cesium *n*-hexylphoshonate (CsHPA, at 20 kHz MAS), oleylammonium *n*-hexylphosphonate (OLAHPA, at 20 kHz MAS). (d) ^{133}Cs MAS NMR spectra of HPA-capped $CsPbBr_3$ NPLs, microcrystalline $CsPbBr_3$ (μ-$CsPbBr_3$), and cesium hexylphosphonate (CsHPA).

previously observed for similar phosphonate ligands bound to nanoparticles.[20]

In order to shed light on the local structure of HPA-NPLs in the solid state, we carried out solid-state MAS NMR measurements on dried HPA-NPL powder. We first identify the residual long-chain aliphatic ligand present on the surface using ^{1}H−^{13}C cross-polarization (CP)[39] MAS NMR (Figure 2b). The aliphatic chain of HPA is expected to give resonances between 15 and 40 ppm. However, the carbon directly bonded to the $-NH_3^+$ group is strongly deshielded (shifted to higher ppm values) and yields a characteristic, well-resolved peak at 42.4 ppm, confirming the presence of residual OLA ligands on the surface. We did not detect any carbonyl (C=O) groups which are a fingerprint of OA, and thus, we conclude that there is negligible residual OA present on the surface.

In turn, we probe the surface phosphonate ligands in HPA-NPLs in the solid state using ^{1}H−^{31}P CP MAS NMR (Figure 2c). The ^{1}H−^{31}P MAS NMR spectrum of HPA-NPLs yields four peaks at 31.6 ppm (fwhm ∼270 Hz, contributes 49%), 29.8 ppm (fwhm ∼980 Hz, contributes 5%), 25.7 ppm (fwhm ∼270 Hz, contributes 28%), and 24.9 ppm (fwhm ∼240 Hz, contributes 18%) (Figure S8). While CP spectra are in general not quantitative, we find that the directly detected quantitative ^{31}P spectrum yields similar relative intensities (Figure S9). The phosphonate species present in HPA-NPLs do not correspond to neat HPA, cesium phosphonate (CsHPA, 19.5 and 23.4 ppm), or oleylammonium phosphonate (OLAHPA, 20.4 and 28.0 ppm). We therefore conclude that these peaks arise from phosphonate species present in various binding modes on the surface of HPA-NPLs. Similar structural complexity of surface-bonded ligands has been previously observed in trimethylphosphine-capped ZnO[40] and trioctylphosphine-capped CdSe/CdTe nanocrystals.[41] The different phosphonate environments may be associated with the various well-defined facets of HPA-NPLs and different modes of binding of this potentially tridentate ligand. However, we note that the accuracy of current state-of-the-art DFT methods for heteronuclear chemical shift calculation is on the same order of magnitude as the ^{31}P peak separation observed here (∼5−10 ppm[42]), and thus, unambiguous assignment of the binding modes is not yet achievable.

We next employ ^{133}Cs MAS NMR to characterize the perovskite component of HPA-NPLs (Figure 2d). The quantitative ^{133}Cs spectrum of HPA-NPLs contains a broad convolution of resonances spanning the region between 60 and 100 ppm and is shifted to lower frequencies (ppm values) with respect to bulk microcrystalline $CsPbBr_3$ (101.7 ppm). While the nonperovskite phase of cesium hexylphosphonate (CsHPA) yields a ^{133}Cs spectrum which partially overlaps with that of HPA-NPLs, the ^{31}P spectrum (Figure 2c) confirmed the absence of this impurity phase; thus, we conclude that the broad convolution of components indeed belongs to HPA-NPLs. Broad NMR resonances in semiconductor nanocrystals are expected because of the high extent of local disorder and may be caused by the anisotropic shape of the nanocrystal.[36,37] The distinct components likely correspond to cesium sites inside the NPL and on or close to the surface of the 3 unique types of NPL facets (see Figure S10 and Supplementary Note 1). Analogous relations between spatial position and NMR shift have been previously observed in low-dimensional ZnSe.[36] Taken together, the NMR results allow us to (i) confirm the successful purification of HPA-NPLs, (ii) identify the presence of residual OLA on the surface, (iii) establish that HPA-NPL binding involves multiple binding modes, and (iv) determine that the local structure of the perovskite component is highly heterogeneous owing to the anisotropic shape of NPLs.

It is widely accepted that the detachment of ligands causes $CsPbBr_3$ NPLs to coalesce, leading to a loss of quantum confinement.[14,15] In order to monitor spectral stability of NPL solutions, we employed hyperspectral wide-field microscopy to spatially map the PL from thin films deposited from the solutions. This technique allows us to acquire PL maps at different wavelengths as well as broadband emission. We start with OLA-NPLs wherein an NPL solution is characterized by a pure blue emission at 448 nm as a result of strong confinement (see Figure S3). This material presents a dominant emission line at 448 nm when deposited by spin coating. However, we also observe many regions on the sample which show emission from green impurities at approximately 510 nm (Figure 3a). We interpret this result as being due to the weak character of

https://dx.doi.org/10.1021/acsenergylett.0c00935
ACS Energy Lett. 2020, 5, 1900−1907

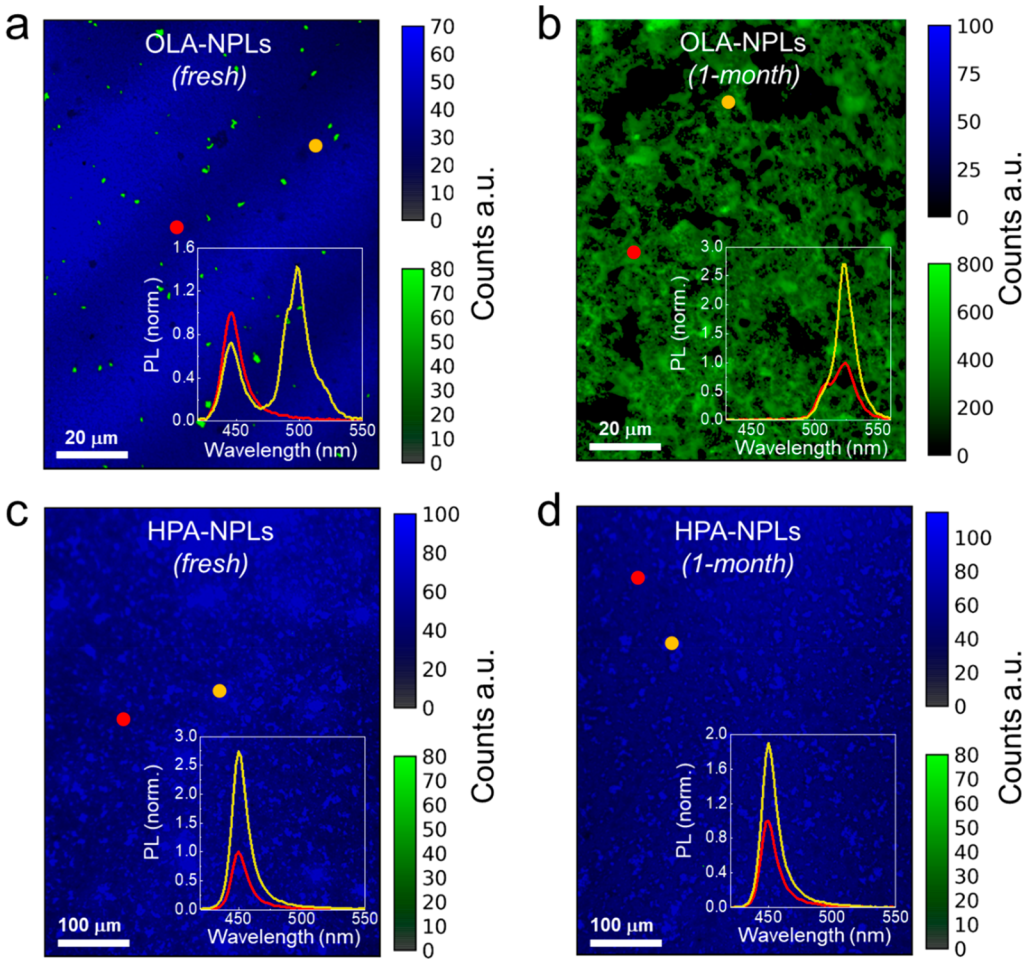

Figure 3. Wide-field hyperspectral PL microscopy characterization of films cast from fresh and aged NPL solutions, with excitation at 405 nm (~10 mW/cm^2). PL maps from thin films deposited from (a) fresh OLA-NPL solution, (b) 1 month aged OLA-NPL solution, (c) fresh HPA-NPL solution, and (d) 1 month aged HPA-NPL solution. The blue color map shows the emission of the confined NPLs averaged between 440 and 460 nm. The green color scale shows the emission of the coalesced NPLs averaged from 490 to 510 nm. Insets display the normalized PL spectra from selected areas as indicated by the colored circles.

the ligand giving rise to coalescence of the NPLs at specific regions even in these freshly made and deposited samples; such coalescence effects become further exaggerated with aging (Figure 3b).[15] By contrast, we do not observe such green emission when we employ HPA to synthesize the NPLs (Figure 3c). We note that the observed spatial differences in the PL intensity throughout the material are likely caused by precipitation of the HPA-NPLs owing to the short length of the ligand, which results in the formation of micrometer-size agglomerated NPLs (see reflectance images taken from the same areas in Figure S11). Even in spite of such heterogeneous morphology, the HPA-NPL film shows no observable green impurity.

We now assess the stability of the HPA-NPLs in solution over time by mapping the PL of thin films after aging the NPL solution for 1 week (Figure S12) and 1 month (Figure 3d) in ambient air (see Figure S13 for corresponding plots of the average PL wavelength of each sample). We do not see any evidence of coalescence (i.e., spectral PL shifts) or substantial PL quenching (small reduction of PLQY from 40% to 34% after 1 month), revealing excellent long-term stability of the HPA-NPL solutions. These observations are consistent with the strong binding affinity of the phosphonate ligands to the surface of anisotropic NPLs and inhibition of coalescence in the HPA-NPL solutions.

Next, we evaluate the stability of the NPL thin films under continuous photoinjection of charge carries, i.e., under continuous illumination (see Figure S14 for initial UV−Vis spectra). We show in Figure 4a the PL spectra recorded from an OLA-NPL film during 30 min of exposure to 400 nm excitation at ~50 mW/cm^2 (equivalent to an LED running at ~16 mA/cm^2) under ambient laboratory conditions. Initially, an emission peak at 450 nm with a shoulder in the green range is observed. With increasing exposure time, the blue emission reduces concomitant with the growth of a longer-wavelength peak that strongly increases in intensity until its center approaches approximately 515 nm. We note that encapsulated OLA-NPL samples exhibit similar PL changes albeit with slower transformation (see Figure S15). Such observations are consistent with previous studies on OLA-NPLs which undergo a transformation from blue-emitting NPLs to green-emitting nanobelts in similar ambient conditions under UV light illumination.[27] By contrast, the HPA-NPLs preserve their pure blue emission (PL peak at ~450 nm) under these same illumination conditions in ambient atmosphere (Figure 4b). In fact, even after 960 min (16 h) of illumination, no green emission is observed (Figure 4b, dashed line). We observe that

https://dx.doi.org/10.1021/acsenergylett.0c00935
ACS Energy Lett. 2020, 5, 1900−1907

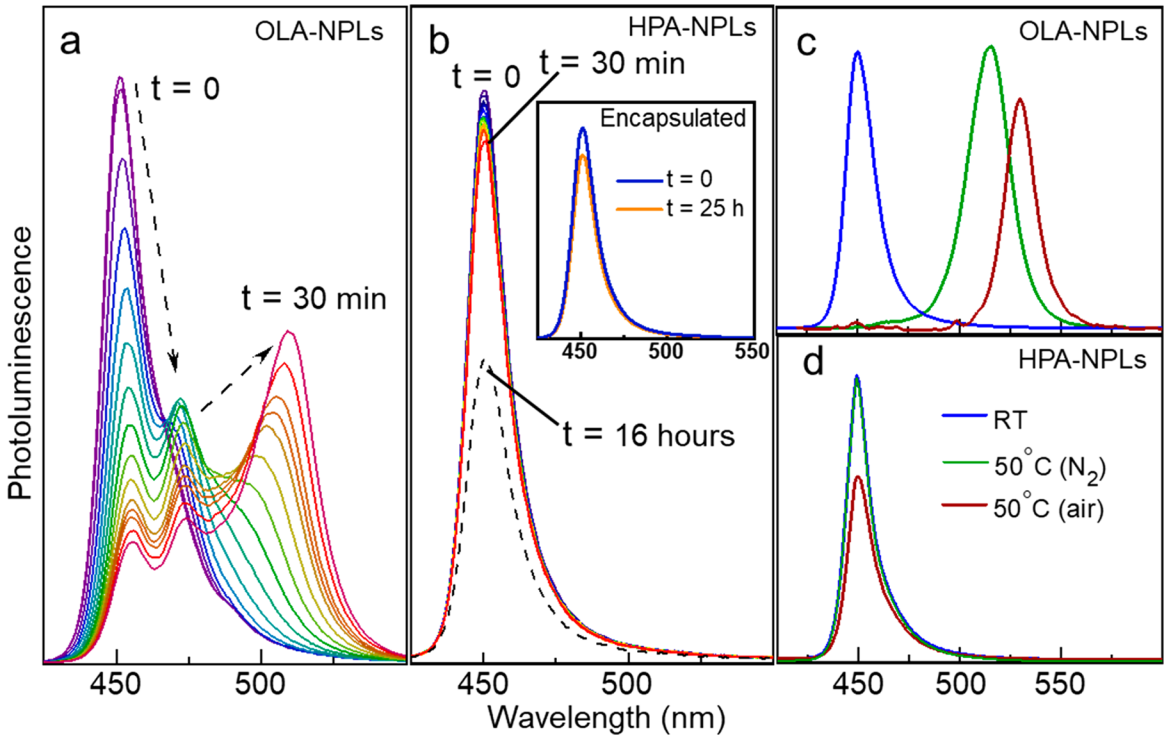

Figure 4. (a and b) PL spectra from NPL thin films under continuous illumination (400 nm, 50 mW/cm^2) in air over a period of 30 min: (a) OLA-NPL and (b) HPA-NPL thin films (time step of 2 min). The dashed line in panel b represents the PL of HPA-NPLs after 16 h of illumination. The inset shows PL spectra from a HPA-NPL film encapsulated by a glass slide in nitrogen before and after 25 h of illumination. (c an, d) Thermal stability: PL spectra of (c) OLA-NPL and (d) HPA-NPL thin films after heating at 50 °C for 30 min in the stated atmosphere (RT refers to room temperature without any heat treatment).

the PL intensity drops to ∼50% of its starting value for the measurements in ambient laboratory air, though this drop is substantially reduced if the HPA-NPL film is encapsulated by a glass slide in nitrogen prior to the measurement (Figure 4b inset). Even after 25 h of continuous light exposure, the PL signal is maintained at 450 nm without any evidence of the green color impurity, and the PL intensity decreases only slightly (<10%). We further tested the encapsulated HPA-NPLs by wide-field hyperspectral imaging at higher photo-excitation intensities equivalent to LED currents between 3.5 and 3500 mA/cm^2 at 405 nm and do not see any evidence of the green impurity or degradation on the microscale (Figure S16).

To assess the thermal stability of the films, we monitored the PL from OLA-NPL and HPA-NPL thin films before and after heating the samples. For the OLA-NPL thin film, there is a clear shift in the emission wavelength to 515 nm after 30 min of annealing at 50 °C in a nitrogen glovebox (Figure 4c), and this shift is even further exaggerated when heating in air (530 nm, Figure 4c). By contrast, the HPA-NPL film preserves its blue emission energy under the same conditions (Figure 4d). In fact, the blue emission can be maintained even when heating the HPA-NPL films at 80 °C for 60 min in a glovebox, and it is only when performing this heating step in ambient air (without any protection from oxygen or water molecules) do we start to observe a shift in PL for these passivated samples (Figure S17).

Finally, to understand the structural and electronic properties of the HPA-NPLs, we performed density functional theory (DFT) calculations. An NPL of 4 atomic layers was created to represent the pseudo-2D NPLs synthesized in the experiments, with the top and bottom surfaces being the {100} facets terminated by a CsBr layer (further computational details are provided in the Supporting Information). The top surfaces were passivated with short methyl ammonium ($CH_3NH_3^+$) and methyl phosphonate ($CH_3PO_3H^-$) molecules to model the long-chained OLA and HPA, respectively (Figure 5a,b). The NPLs considered in the calculations are trap-free, and the valence band maximum (VBM) and conduction band minimum (CBM) states are delocalized (Figure S18). The binding affinity (E_{bind})[20] of the ligands to the NPL surface is computed as

$$E_{bind} = E_{tot} - E_V - E_{ligand}$$

where E_{tot} is the energy of the NPL fully passivated with ligands, E_V the energy of the NPL with a vacancy, and E_{ligand} the energy of the ligand and counterion pair. Here, the vacancies are the methylammonium ligand with a Br^- counterion and the methyl phosphonate ligand with a Cs^+ counterion. The E_{bind} of the phosphonate ligand is ∼0.64 eV, whereas that of the amine is only ∼0.31 eV per molecule. Furthermore, there is greater overlap between the total electron density of the methyl phosphonate ligand with the NPL (Figure 5d), compared to that of the amine (Figure 5c). We propose that the much stronger binding affinity explains the high resilience against coalescence, and hence enhanced optical and thermal stability, of the HPA-NPLs compared to OLA-NPLs. Furthermore, the enhanced binding and different binding mechanism of the HPA ligands is consistent with a change in the intrinsic material properties reflected in, for example, the observed increased radiative rate of recombination.

https://dx.doi.org/10.1021/acsenergylett.0c00935
ACS Energy Lett. 2020, 5, 1900−1907

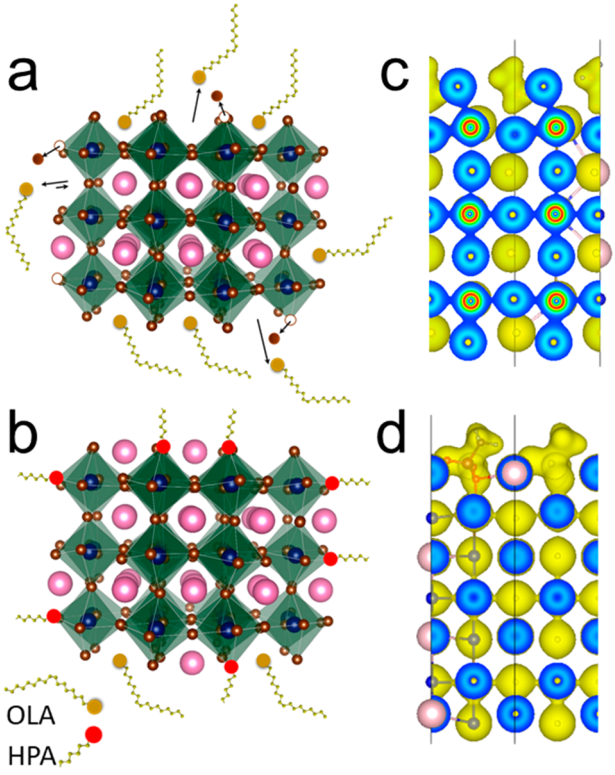

Figure 5. DFT calculations. (a and b) Schematics showing the binding of the protonated amine (OLA^+) and deprotonated phosphonate on the NPL surface. The Cs, Pb, and Br atoms are denoted by pink, blue, and brown spheres. (c and d) The total electron density (denoted as yellow isosurfaces) of the NPLs passivated with methyl amine and methyl phosphonate ligands.

These results represent important breakthroughs for device integration and performance. The high temperature threshold of degradation (>80 °C in inert conditions) is compatible with standard LED device processing and operation temperatures. Furthermore, their stability validation under LED-like operation conditions shows promise for fabricating blue LEDs with stable color and emission yield using nanostructured perovskite systems, which has remained elusive. Light-emission device integration will require further focus on optimization of contacts, deposition, and ligand length, among other factors. By developing such robust chemical strategies to fabricate materials operating with high radiative efficiencies, further studies into other high-efficiency optoelectronic devices also become feasible.

In conclusion, we have developed a new *in situ* passivation strategy to synthesize color-pure blue-emitting quantum-confined $CsPbBr_3$ NPLs. We confirmed the surface-binding of the phosphonate ligands through solid-state NMR. The as-prepared HPA-NPL thin films present PLQY of 40% with emission peak at 450 nm in solid state, which is preserved after one month of storage in ambient air conditions. Using macroscopic and hyperspectral wide-field PL microscopy, we showed that the HPA-NPLs exhibit excellent spectral and thermal stability over time and under device-like operating conditions through photoinjection of carriers. We attribute these results to the stronger binding affinity of HPA to the surface of $CsPbBr_3$ NPLs as ascertained by DFT calculations. Our work thus sheds new light on the challenges for translating the high performance of quantum-confined NPLs in solution to those in solid films for next-generation lighting and quantum technologies.

■ ASSOCIATED CONTENT

Supporting Information

The Supporting Information is available free of charge at https://pubs.acs.org/doi/10.1021/acsenergylett.0c00935.

Experimental details of the syntheses of NPLs; characterization details, TEM, and optical data of OLA-NPLs; PL decay of OLA- and HPA-NPLs; supporting NMR data; reflectance images of OLA- and HPA-NPL films; PL map of HPA-NPL film after 1 week; optical instability of encapsulated OLA-NPL thin film; thermal stability of HPA-NPLs at 80 °C; details of DFT calculations (PDF)

■ AUTHOR INFORMATION

Corresponding Author

Samuel D. Stranks − *Cavendish Laboratory and Department of Chemical Engineering & Biotechnology, University of Cambridge, Cambridge CB3 0HE, United Kingdom;* orcid.org/0000-0002-8303-7292; Email: sds65@cam.ac.uk

Authors

Javad Shamsi − *Cavendish Laboratory, University of Cambridge, Cambridge CB3 0HE, United Kingdom;* orcid.org/0000-0003-4684-5407

Dominik Kubicki − *Cavendish Laboratory and Department of Chemistry, University of Cambridge, Cambridge CB3 0HE, United Kingdom;* orcid.org/0000-0002-9231-6779

Miguel Anaya − *Cavendish Laboratory, University of Cambridge, Cambridge CB3 0HE, United Kingdom;* orcid.org/0000-0002-0384-5338

Yun Liu − *Cavendish Laboratory, University of Cambridge, Cambridge CB3 0HE, United Kingdom;* orcid.org/0000-0003-1630-4052

Kangyu Ji − *Cavendish Laboratory, University of Cambridge, Cambridge CB3 0HE, United Kingdom*

Kyle Frohna − *Cavendish Laboratory, University of Cambridge, Cambridge CB3 0HE, United Kingdom*

Clare P. Grey − *Department of Chemistry, University of Cambridge, Cambridge CB2 1EW, United Kingdom;* orcid.org/0000-0001-5572-192X

Richard H. Friend − *Cavendish Laboratory, University of Cambridge, Cambridge CB3 0HE, United Kingdom;* orcid.org/0000-0001-6565-6308

Complete contact information is available at: https://pubs.acs.org/10.1021/acsenergylett.0c00935

Notes

The authors declare no competing financial interest.

■ ACKNOWLEDGMENTS

J.S. and S.D.S. acknowledge the European Research Council (ERC) under the European Union's Horizon 2020 research and innovation program (HYPERION, Grant Agreement Number 756962). S.D.S acknowledges funding from the Royal Society and Tata Group (UF150033). R.H.F. and Y.L. acknowledge support from the Simons Foundation (Grant 601946). M.A. and D.K. acknowledge funding from the European Union's Horizon 2020 research and innovation

https://dx.doi.org/10.1021/acsenergylett.0c00935
ACS Energy Lett. 2020, 5, 1900−1907

programme under the Marie Skłodowska-Curie (Grant Agreement Number 841386 and 841136, respectively). K.J. acknowledges funding from the Royal Society (RGFR1180002). K.F. acknowledges a George and Lilian Schiff Studentship, Winton Studentship, the Engineering and Physical Sciences Research Council (EPSRC) studentship, Cambridge Trust Scholarship, and Robert Gardiner Scholarship. C.P.G. acknowledges the European Research Council (ERC) under the European Union's Horizon 2020 research and innovation program (835073) and the Royal Society for a Research Professorship (RP\R1\180147). The authors acknowledge the EPSRC for funding (EP/R023980/1).

REFERENCES

(1) Nakamura, S. Background Story of the Invention of Efficient InGaN Blue-Light-Emitting Diodes (Nobel Lecture). *Angew. Chem., Int. Ed.* **2015**, *54* (27), 7770−7788.
(2) Li, C. H. A.; Zhou, Z.; Vashishtha, P.; Halpert, J. E. The Future Is Blue (LEDs): Why Chemistry Is the Key to Perovskite Displays. *Chem. Mater.* **2019**, *31* (16), 6003−6032.
(3) Kovalenko, M. V.; Protesescu, L.; Bodnarchuk, M. I. Properties and Potential Optoelectronic Applications of Lead Halide Perovskite Nanocrystals. *Science* **2017**, *358* (6364), 745−750.
(4) Akkerman, Q. A.; Raino, G.; Kovalenko, M. V.; Manna, L. Genesis, Challenges and Opportunities for Colloidal Lead Halide Perovskite Nanocrystals. *Nat. Mater.* **2018**, *17* (5), 394−405.
(5) Shamsi, J.; Urban, A. S.; Imran, M.; De Trizio, L.; Manna, L. Metal Halide Perovskite Nanocrystals: Synthesis, Post-Synthesis Modifications, and Their Optical Properties. *Chem. Rev.* **2019**, *119* (5), 3296−3348.
(6) Stranks, S. D.; Snaith, H. J. Metal-Halide Perovskites for Photovoltaic and Light-Emitting Devices. *Nat. Nanotechnol.* **2015**, *10* (5), 391−402.
(7) Yan, F.; Tan, S. T.; Li, X.; Demir, H. V. Light Generation in Lead Halide Perovskite Nanocrystals: LEDs, Color Converters, Lasers, and Other Applications. *Small* **2019**, *15* (47), 1902079.
(8) Quan, L. N.; García de Arquer, F. P.; Sabatini, R. P.; Sargent, E. H. Perovskites for Light Emission. *Adv. Mater.* **2018**, *30* (45), 1801996.
(9) Veldhuis, S. A.; Boix, P. P.; Yantara, N.; Li, M.; Sum, T. C.; Mathews, N.; Mhaisalkar, S. G. Perovskite Materials for Light-Emitting Diodes and Lasers. *Adv. Mater.* **2016**, *28* (32), 6804−6834.
(10) Weidman, M. C.; Seitz, M.; Stranks, S. D.; Tisdale, W. A. Highly Tunable Colloidal Perovskite Nanoplatelets through Variable Cation, Metal, and Halide Composition. *ACS Nano* **2016**, *10* (8), 7830−7839.
(11) MacLaughlin, C. M. Opportunities and Challenges in Perovskite-Based Display Technologies: A Conversation with Andrey Rogach and Haibo Zeng. *Acs Energy Lett.* **2019**, *4* (4), 977−979.
(12) Bohn, B. J.; Tong, Y.; Gramlich, M.; Lai, M. L.; Doblinger, M.; Wang, K.; Hoye, R. L. Z.; Muller-Buschbaum, P.; Stranks, S. D.; Urban, A. S.; Polavarapu, L.; Feldmann, J. Boosting Tunable Blue Luminescence of Halide Perovskite Nanoplatelets through Post-synthetic Surface Trap Repair. *Nano Lett.* **2018**, *18* (8), 5231−5238.
(13) Wu, Y.; Wei, C.; Li, X.; Li, Y.; Qiu, S.; Shen, W.; Cai, B.; Sun, Z.; Yang, D.; Deng, Z.; Zeng, H. In Situ Passivation of PbBr64− Octahedra toward Blue Luminescent CsPbBr3 Nanoplatelets with Near 100% Absolute Quantum Yield. *ACS Energy Lett.* **2018**, *3* (9), 2030−2037.
(14) Wang, Y.; Li, X.; Sreejith, S.; Cao, F.; Wang, Z.; Stuparu, M. C.; Zeng, H.; Sun, H. Photon Driven Transformation of Cesium Lead Halide Perovskites from Few-Monolayer Nanoplatelets to Bulk Phase. *Adv. Mater.* **2016**, *28* (48), 10637−10643.
(15) Dang, Z.; Dhanabalan, B.; Castelli, A.; Dhall, R.; Bustillo, K. C.; Marchelli, D.; Spirito, D.; Petralanda, U.; Shamsi, J.; Manna, L.; Krahne, R.; Arciniegas, M. P. Temperature Driven Transformation of CsPbBr3 Nanoplatelets into Mosaic Nanotiles in Solution through Self-Assembly. *Nano Lett.* **2020**, *20* (3), 1808−1818.
(16) Gomez, L.; Lin, J.; de Weerd, C.; Poirier, L.; Boehme, S. C.; von Hauff, E.; Fujiwara, Y.; Suenaga, K.; Gregorkiewicz, T. Extraordinary Interfacial Stitching between Single All-Inorganic Perovskite Nanocrystals. *ACS Appl. Mater. Interfaces* **2018**, *10* (6), 5984−5991.
(17) Yassitepe, E.; Yang, Z.; Voznyy, O.; Kim, Y.; Walters, G.; Castañeda, J. A.; Kanjanaboos, P.; Yuan, M.; Gong, X.; Fan, F.; Pan, J.; Hoogland, S.; Comin, R.; Bakr, O. M.; Padilha, L. A.; Nogueira, A. F.; Sargent, E. H. Amine-Free Synthesis of Cesium Lead Halide Perovskite Quantum Dots for Efficient Light-Emitting Diodes. *Adv. Funct. Mater.* **2016**, *26* (47), 8757−8763.
(18) Almeida, G.; Goldoni, L.; Akkerman, Q.; Dang, Z.; Khan, A. H.; Marras, S.; Moreels, I.; Manna, L. Role of Acid-Base Equilibria in the Size, Shape, and Phase Control of Cesium Lead Bromide Nanocrystals. *ACS Nano* **2018**, *12* (2), 1704−1711.
(19) Akkerman, Q. A.; Motti, S. G.; Srimath Kandada, A. R.; Mosconi, E.; D'Innocenzo, V.; Bertoni, G.; Marras, S.; Kamino, B. A.; Miranda, L.; De Angelis, F.; Petrozza, A.; Prato, M.; Manna, L. Solution Synthesis Approach to Colloidal Cesium Lead Halide Perovskite Nanoplatelets with Monolayer-Level Thickness Control. *J. Am. Chem. Soc.* **2016**, *138* (3), 1010−1016.
(20) Zhang, B.; Goldoni, L.; Zito, J.; Dang, Z.; Almeida, G.; Zaccaria, F.; de Wit, J.; Infante, I.; De Trizio, L.; Manna, L. Alkyl Phosphonic Acids Deliver CsPbBr3 Nanocrystals with High Photoluminescence Quantum Yield and Truncated Octahedron Shape. *Chem. Mater.* **2019**, *31* (21), 9140−9147.
(21) Tan, Y.; Zou, Y.; Wu, L.; Huang, Q.; Yang, D.; Chen, M.; Ban, M.; Wu, C.; Wu, T.; Bai, S.; Song, T.; Zhang, Q.; Sun, B. Highly Luminescent and Stable Perovskite Nanocrystals with Octylphosphonic Acid as a Ligand for Efficient Light-Emitting Diodes. *ACS Appl. Mater. Interfaces* **2018**, *10* (4), 3784−3792.
(22) Koh, W.; Park, S.; Ham, Y. Phosphonic Acid Stabilized Colloidal CsPbX3(X = Br, I) Perovskite Nanocrystals and Their Surface Chemistry. *ChemistrySelect* **2016**, *1* (13), 3479−3482.
(23) Smock, S. R.; Williams, T. J.; Brutchey, R. L. Quantifying the Thermodynamics of Ligand Binding to CsPbBr3 Quantum Dots. *Angew. Chem., Int. Ed.* **2018**, *57* (36), 11711−11715.
(24) Imran, M.; Ijaz, P.; Baranov, D.; Goldoni, L.; Petralanda, U.; Akkerman, Q. A.; Abdelhady, A. L.; Prato, M.; Bianchini, P.; Infante, I.; Manna, L. Shape Pure, Nearly Monodisperse CsPbBr3 Nanocubes Prepared Using Secondary Aliphatic Amines. *Nano Lett.* **2018**, *18* (12), 7822−7831.
(25) Krieg, F.; Ong, Q. K.; Burian, M.; Raino, G.; Naumenko, D.; Amenitsch, H.; Süess, A.; Grotevent, M.; Krumeich, F.; Bodnarchuk, M. I.; Shorubalko, I.; Stellacci, F.; Kovalenko, M. V. Stable Ultra-Concentrated and Ultra-Dilute Colloids of CsPbX3 (X = Cl, Br) Nanocrystals Using Natural Lecithin as a Capping Ligand. *J. Am. Chem. Soc.* **2019**, *141* (50), 19839−19849.
(26) Shynkarenko, Y.; Bodnarchuk, M. I.; Bernasconi, C.; Berezovska, Y.; Verteletskyi, V.; Ochsenbein, S.; Kovalenko, M. V. Direct Synthesis of Quaternary Alkylammonium Capped Perovskite Nanocrystals for Efficient Blue and Green Light-Emitting Diodes. *ACS Energy Lett.* **2019**, *4* (11), 2703−2711.
(27) Shamsi, J.; Rastogi, P.; Caligiuri, V.; Abdelhady, A. L.; Spirito, D.; Manna, L.; Krahne, R. Bright-Emitting Perovskite Films by Large-Scale Synthesis and Photoinduced Solid-State Transformation of CsPbBr3 Nanoplatelets. *ACS Nano* **2017**, *11* (10), 10206−10213.
(28) Almeida, G.; Infante, I.; Manna, L. Resurfacing Halide Perovskite Nanocrystals. *Science* **2019**, *364* (6443), 833−834.
(29) Sun, S.; Yuan, D.; Xu, Y.; Wang, A.; Deng, Z. Ligand-Mediated Synthesis of Shape-Controlled Cesium Lead Halide Perovskite Nanocrystals via Reprecipitation Process at Room Temperature. *ACS Nano* **2016**, *10* (3), 3648−3657.
(30) Bertolotti, F.; Nedelcu, G.; Vivani, A.; Cervellino, A.; Masciocchi, N.; Guagliardi, A.; Kovalenko, M. V. Crystal Structure, Morphology and Surface Termination of Cyan-Emissive, 6-Monolayers-Thick CsPbBr3 Nanoplatelets from X-Ray Total Scattering. *ACS Nano* **2019**, *13* (12), 14294−14307.

https://dx.doi.org/10.1021/acsenergylett.0c00935
ACS Energy Lett. 2020, 5, 1900−1907

(31) Lao, X. Z.; Yang, Z.; Su, Z. C.; Wang, Z.; Ye, H.; Wang, M.; yao, xi; Xu, S. J. Luminescence and Thermal Behaviors of Free and Trapped Excitons in Cesium Lead Halide Perovskite Nanosheets. *Nanoscale* **2018**, *10*, 9949.
(32) Van Gompel, W. T. M.; Herckens, R.; Reekmans, G.; Ruttens, B.; D'Haen, J.; Adriaensens, P.; Lutsen, L.; Vanderzande, D. Degradation of the Formamidinium Cation and the Quantification of the Formamidinium-Methylammonium Ratio in Lead Iodide Hybrid Perovskites by Nuclear Magnetic Resonance Spectroscopy. *J. Phys. Chem. C* **2018**, *122*, 4117−4124.
(33) Kubicki, D. J.; Prochowicz, D.; Hofstetter, A.; Zakeeruddin, S. M.; Grätzel, M.; Emsley, L. Phase Segregation in Cs-, Rb- and K-Doped Mixed-Cation (MA)x(FA)1−XPbI3 Hybrid Perovskites from Solid-State NMR. *J. Am. Chem. Soc.* **2017**, *139* (40), 14173−14180.
(34) Rosales, B. A.; Men, L.; Cady, S. D.; Hanrahan, M. P.; Rossini, A. J.; Vela, J. Persistent Dopants and Phase Segregation in Organolead Mixed-Halide Perovskites. *Chem. Mater.* **2016**, *28*, 6848−6859.
(35) Franssen, W. M. J.; Kentgens, A. P. M. Solid−State NMR of Hybrid Halide Perovskites. *Solid State Nucl. Magn. Reson.* **2019**, *100*, 36−44.
(36) Cadars, S.; Smith, B. J.; Epping, J. D.; Acharya, S.; Belman, N.; Golan, Y.; Chmelka, B. F. Atomic Positional Versus Electronic Order in Semiconducting ZnSe Nanoparticles. *Phys. Rev. Lett.* **2009**, *103* (13), 136802.
(37) Piveteau, L.; Ong, T.-C.; Rossini, A. J.; Emsley, L.; Copéret, C.; Kovalenko, M. V. Structure of Colloidal Quantum Dots from Dynamic Nuclear Polarization Surface Enhanced NMR Spectroscopy. *J. Am. Chem. Soc.* **2015**, *137* (43), 13964−13971.
(38) Hanrahan, M. P.; Chen, Y.; Blome-Fernández, R.; Stein, J. L.; Pach, G. F.; Adamson, M. A. S.; Neale, N. R.; Cossairt, B. M.; Vela, J.; Rossini, A. J. Probing the Surface Structure of Semiconductor Nanoparticles by DNP SENS with Dielectric Support Materials. *J. Am. Chem. Soc.* **2019**, *141* (39), 15532−15546.
(39) Pines, A.; Gibby, M. G.; Waugh, J. S. Proton-Enhanced NMR of Dilute Spins in Solids. *J. Chem. Phys.* **1973**, *59*, 569−590.
(40) Peng, Y.-K.; Ye, L.; Qu, J.; Zhang, L.; Fu, Y.; Teixeira, I. F.; McPherson, I. J.; He, H.; Tsang, S. C. E. Trimethylphosphine-Assisted Surface Fingerprinting of Metal Oxide Nanoparticle by 31P Solid-State NMR: A Zinc Oxide Case Study. *J. Am. Chem. Soc.* **2016**, *138* (7), 2225−2234.
(41) Ratcliffe, C. I.; Yu, K.; Ripmeester, J. A.; Badruz Zaman, Md.; Badarau, C.; Singh, S. Solid State NMR Studies of Photoluminescent Cadmium Chalcogenide Nanoparticles. *Phys. Chem. Chem. Phys.* **2006**, *8* (30), 3510−3519.
(42) Paruzzo, F. M.; Hofstetter, A.; Musil, F.; De, S.; Ceriotti, M.; Emsley, L. Chemical Shifts in Molecular Solids by Machine Learning. *Nat. Commun.* **2018**, *9* (1), 1−10.

https://dx.doi.org/10.1021/acsenergylett.0c00935
ACS Energy Lett. 2020, 5, 1900−1907